An integrated electroactive polymer sensor–actuator: design, model-based control, and performance characterization

2016 Smart Mater. Struct. 25 035016

(http://iopscience.iop.org/0964-1726/25/3/035016)

IOP Publishing Smart Materials and Structures
Smart Mater. Struct. 25 (2016) 035016 (16pp) doi:10.1088/0964-1726/25/3/035016

An integrated electroactive polymer sensor–actuator: design, model-based control, and performance characterization

A Hunt[1], Z Chen[2], X Tan[3] and M Kruusmaa[1]

[1] Centre for Biorobotics, Department of Information Technology, Tallinn University of Technology, Akadeemia tee 15A-111, 12618 Tallinn, Estonia
[2] Department of Electrical Engineering and Computer Science, Wichita State University, 252 Jabara Hall, 1845 Fairmount St. Wichita, KS 67260, USA
[3] Department of Electrical & Computer Engineering, Michigan State University, 428 S. Shaw Lane, 2120 Engineering Building, East Lansing, MI 4882 USA

E-mail: Andres.Hunt@ttu.ee

Received 11 August 2015, revised 24 January 2016
Accepted for publication 29 January 2016
Published 22 February 2016

Abstract

Ionic electroactive polymers (IEAPs), particularly ionic polymer-metal composites (IPMCs) and carbon-polymer composites (CPCs), bend when a voltage is applied on their electrodes, and conversely, they generate an electrical signal when subjected to a mechanical bending. In this work we study and compare the capabilities of IPMC and CPC actuators and sensors in closed-loop control applications. We propose and realize an integrated IEAP sensor–actuator design, characterize its performance using three different materials, and compare the results. The design consists of two short IEAP actuators and one sensor mechanically coupled together in a parallel configuration, and an attached rigid extension significantly longer than the IEAPs. This allows the device to be compliant, simple to construct, lightweight, easy to miniaturize, and functionally similar to a one-degree-of-freedom rotational joint. For control design and accurate position sensing in feedback experiments, we adapt physics-based and control-oriented models of actuation and sensing dynamics, and perform experiments to identify their parameters. In performance characterization, both model-based H_∞ control and proportional-integral control are explored. System responses to step inputs, sinusoids, and random references are measured, and long-duration sinusoidal tracking experiments are performed. The results show that, while IEAP position sensing is stable for only a limited time-span, H_∞ control significantly improves the performance of the device.

Keywords: IPMC, CPC, EAP, actuator, sensor, control, feedback

(Some figures may appear in colour only in the online journal)

1. Introduction

The rapidly advancing field of materials science has introduced many 'smart' materials with novel sensing and actuation capabilities. The ability of electroactive polymer (EAP) materials to change their shapes or sizes under electrical excitation is offering appealing alternatives to conventional sensors and actuators [1]. Two functionally similar classes of such materials are ionic polymer-metal composites (IPMCs) [2] and carbon-polymer-composites (CPCs) [3]. Both are ionic electroactive polymers (IEAPs) that change their curvature when a voltage is applied across their electrodes and conversely, generate an electrical signal when they are bent. Since their first introduction over two decades ago [4], their properties have been greatly improved, e.g., both the power consumption and surface resistance have been significantly reduced [5].

IEAP materials have been proposed for various applications in the field of robotics [6] due to their technological potential and advantages over conventional actuators,

including easy scalability, light weight, and low actuation voltage, to name a few. Robotic fish propulsion [7–9], heart rate monitoring [10], embryo injection [11], linked manipulator [12], seismic sensor [13] and artificial lateral line [14] are some examples of reported studies on exploiting IEAPs. Thorough overviews on the materials and their proposed applications can be found in [15–17].

In some applications (e.g. robotic fish propulsion) the actuator performs well in the open-loop configuration. However, feedback is often desirable to further improve the performance. In this regard, IEAP self-sensing actuation schemes appear attractive, the implementation of which includes measuring actuator's surface resistance [18], and patterning actuator's electrodes to create resistive sensor areas on its edges [19], among others. Unfortunately, these solutions typically have not been demonstrated to function in feedback configurations. The feedback in IEAP actuator control is most often accomplished using an external sensor, e.g., a camera [20, 21] or a laser distance meter [22–26]. However, such solutions greatly increase the overall size of the system. Some authors have overcome this issue by mechanically integrating various sensors with IEAP actuators. For example, Chen *et al* combined a PVDF sensor with an IPMC actuator [27], and Leang *et al* added a strain gauge on an IPMC actuator's surface [28]. Since these approaches involve bonding of other materials on the IEAP surface, they also add significantly to the stiffness and thus result in reduction in the actuation capabilities.

In addition to the aforementioned reports, there are many other works that implement feedback control on IEAP actuators (e. g. [23, 29–34]), but only a few studies utilize the same materials for providing the feedback signal. For example, Newbury implemented a compensator for controlling oscillations of a rotary device using one IPMC sensor and four IPMC actuators [35]. He reported 1 s long feedback experiment fragments to demonstrate improved performance (over the open-loop configuration) in a narrow frequency interval. Bonomo *et al* [36] attached two identical IPMCs side-by-side to a plastic sheet and fed the amplified voltage signal generated by one IPMC to the other, in order to either suppress (negative feedback) or sustain (positive feedback) the oscillations initiated by an external stimulus. A maximum of 5 s long experiments were reported and the feasibility of the design was qualitatively concluded, based on the IPMC sensor's output voltage in combination with visual observations, while the actual deformations were not measured. Later, Yamakita *et al* [37] presented preliminary results on using IPMCs in parallel for actuation and sensing in precision feedback control. They were able to conduct two experiments using an unspecified setup—tracking a step input and a 0.2 Hz sinusoidal signal, each for 10 s. More recently, Gonzalez *et al* [38] used an IPMC sensor to provide feedback in their work on an IPMC microgripper. They used empirical models and PID control to track step inputs of magnitude from 0.1 to 1 mm, for a maximum of 20 s. The results showed that reaching the reference level takes at least 5 s and for some of the larger amplitudes, it is not possible to reach the reference level. These works did not quantitatively characterize the control precision.

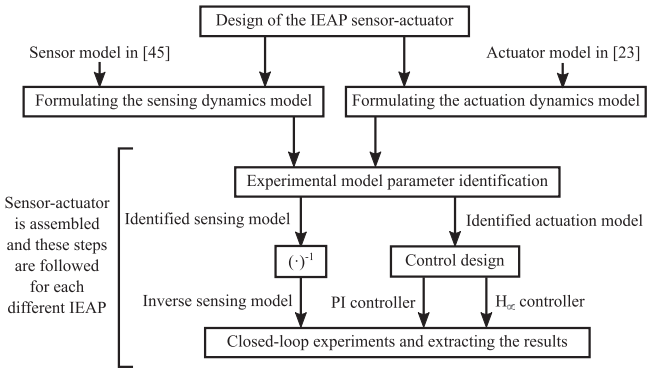

Figure 1. General structure of this work and dependencies between its parts.

In our preliminary work [39] we presented the feedback control of a coupled IPMC sensor–actuator. Empirical models of actuation and sensing dynamics were experimentally identified, a PI controller was designed, and experiments on tracking sinusoidal references were conducted. With IPMC feedback the maximum experiment duration of 120 s was achieved.

In this paper we (1) improve the pivot-like IEAP sensor–actuator design enhancing its actuation capabilities and reducing undesirable twisting motions; (2) model the dynamics of the prototype utilizing physics-based models for IEAP sensing and actuation dynamics; (3) validate the proposed design and quantitatively characterize its performance in model-based feedback control experiments with three different input signals (step, sine, and random references), and an extended (up to 2 h) sine following; (4) compare the results for integrated sensing against external sensing, and PI against H_∞ control, on three identical sensor–actuator prototypes, each constructed utilizing different type of IEAP. An Au-plated IPMC, a Pt-plated IPMC and a CPC material with carbon electrodes are used to obtain a broader comparison between materials similar in construction and function. The general structure of the presented work is illustrated in figure 1. To the best of authors' knowledge this is the first report to achieve up to 30 min long tracking in IEAP sensing feedback configuration (being 90 times longer than reported by other groups), and 2 h long tracking in case of external feedback. Also, the presented quantitative results provide a qualitative 'sense' about the maturity of the IEAP materials for applications.

The rest of this paper is organized as follows. In section 2 we introduce the concept and the prototype of the IEAP sensor–actuator, the IEAP materials, their modelling and control, experimental setup, experimental procedures and evaluation metrics. Section 3 presents the results of model identification and feedback experiments. The results are analysed in section 4 and the conclusions are presented in section 5.

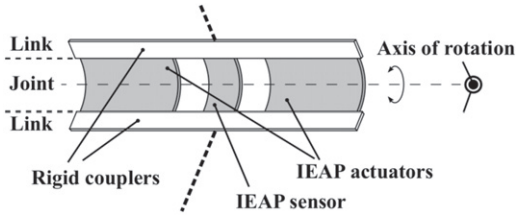

Figure 2. Concept of the proposed IEAP sensor–actuator. The device can be approximated as a rotational joint when the attached rigid links are significantly longer than the IEAPs.

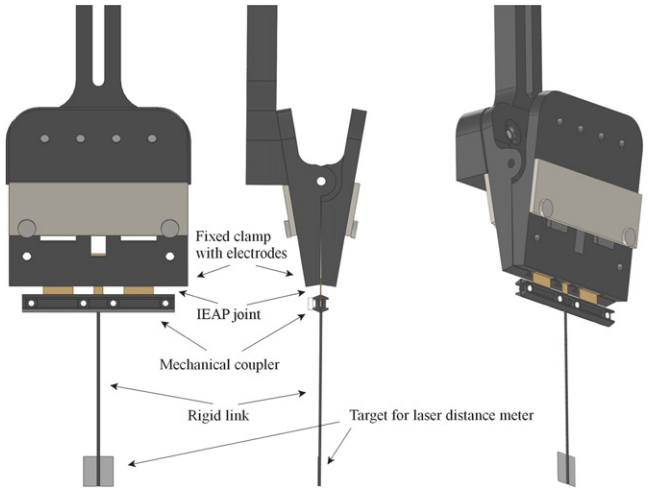

Figure 3. Construction of the proof-of-concept IEAP sensor–actuator prototype used in the experiments.

2. Materials and methods

2.1. The design of the IEAP sensor–actuator

The device consists of IEAPs that are connected in parallel for simultaneous actuation and sensing, with mechanical couplers at both ends, as shown in figure 2. One of the couplers also accommodates terminals connected to IEAP electrodes.

A practical solution for the integrated sensor–actuator used in the experiments in this paper is shown in figure 3. Three IEAP samples are used in parallel—a narrow one in the middle for sensing and two wide ones symmetrically on both sides for actuation. This prevents any potential undesirable twisting during actuation. Short IEAPs are used in the design as they are more efficient than long ones [12, 40], and they allow the sensor to closely follow the shape of the actuator. The resulting behaviour functionally resembles a one-degree-of-freedom rotary joint. On one end the IEAPs are mechanically coupled together using lightweight plastic plates and screws. A carbon fibre rod with a plate on the other end is attached to this coupler so that the motion of its tip can be observed using a laser distance meter. The other end of the IEAP samples is clamped by a spring-loaded plastic clamp with gold-plated silver electrodes. The clamp thus couples the IEAPs mechanically, connects them electrically to sensing or actuation circuits, and fixes that end to the Earth frame during the experiments. Its construction allows one to easily change the sample sets.

The clamp in the fixed end is oriented so that the rotational axis is horizontal and the motion of the extension rod takes place in a vertical plane. In this configuration the IEAPs do not strain due to gravity. The components of the setup such as the clamp are intentionally not miniaturized, as it is not essential for the experiments in this paper. The backbone components of both the clamp and the mechanical coupler are made of ABS plastic using a rapid prototyping machine 3D Touch (3D Systems Inc). All the components of the setup are chemically resistant to water, making it possible to experiment with both wet and dry IEAP materials.

2.2. IPMC and CPC materials

The IPMC and CPC materials consist of a thin membrane sheet (Nafion or Flemion) that is coated with conductive electrodes [2, 3]. Mobile counter-ions are loosely coupled to the ionomer backbone. When a voltage is applied between the electrodes, these counter-ions start migrating in the electric field towards one surface. In the case of Nafion polymer with Li^+ counter-ions, they migrate towards the anode. Actuation voltages vary among materials, but usually are up to 5 V.

IPMCs and CPCs also exhibit sensing properties [41, 42]. Bending an IEAP sheet causes the counter-ion migration within the material due to the pressure gradient across the material thickness. This results in electric potential difference between the surface electrodes; however, the sensing voltages are orders of magnitude smaller than the voltages required for actuation. Typical sensing approaches include measuring the voltage between the electrodes [41, 43] and measuring the sensor charge or current [44–46]. Some IEAPs show a significant change in their surface resistance when bending, which can be used for position sensing, as shown in [18, 19]. We choose to use the IEAP short-circuit current for estimating the material deformation due to its reported high accuracy [45].

In the experiments we use three different IEAP materials that are labelled as material #1, #2 and #3, and respectively we label the sample sets cut from these materials as sample set #1, #2 and #3. Material #1 is made of Nafion^{TM}117 membrane that is coated with coconut shell-derived active carbon electrodes using direct assembly procedure [3]. To enhance the surface conductivity the material is further covered with gold foil and hot-pressed, and immersed in EMI-Tf ionic liquid. The detailed manufacturing procedure is described in [3]. These materials have low surface resistance that varies insignificantly while bending, and they can work well in dry environments due to low vapour pressure of the ionic liquid.

Material #2 is a typical platinum-coated IPMC provided by Environmental Robotics Inc. It is made of Nafion^{TM}117 polymer that is deposited with Pt electrodes using an electroless plating procedure. The loosely coupled hydrogen ions in the polymer are exchanged with larger Li ions.

Material #3 is produced 5 years earlier, similarly as #2, except that the electrodes are made of gold instead of platinum. The functionality of materials #2 and #3 highly depends on their water concentration and they need to be kept

hydrated. The experiments with these materials are conducted in water to prevent water evaporation and guarantee consistent conditions throughout the experiments.

2.3. Model-based feedback control

The interactions among the polymer backbone, ions, and solvent (or ionic liquid) make the IEAP sensing and actuation dynamics complex and the overall behaviour poorly predictable. To a large extent these issues can be overcome with proper modelling and control of the materials. The aim of modelling the IEAP sensing and actuation dynamics in this work is threefold: describing the used materials in terms of their fundamental physical parameters; providing the actuation models for control design; and providing inverse sensing models that relate the IEAP sensor short-circuit current to the actual position of the tip of the sensor–actuator in the closed-loop experiments. Regardless of that many reports have been published on modelling the IEAP sensors and actuators, the actuation and sensing phenomena is yet not fully understood. Multiple potential dominant processes have been proposed, and overviews on modelling can be found in the review papers [16, 17, 47].

In this work we model the sensing and actuation dynamics of the IEAP materials using the Laplace domain models developed by Chen *et al* in [23, 45]. These were originally derived to describe the IPMCs, but are also valid for the functionally identical CPC materials. In particular, it is presumed in the derivation process in [23, 45] that the mechanism behind the actuation and sensing phenomenon is the proportional coupling between the accumulated charge and mechanical stress, while the solvent effects are negligible (see chapter 2 in [45] and chapter II in [23]). Thus, the ionic liquid in CPCs functions both as solvent and counter-ions in IPMCs. Furthermore, the polymer backbone of all IEAPs used in this work is Nafion^{TM}117, and the CPC electrodes (nanoporous carbon covered with gold foil) are equivalent to the coatings of the IPMCs (Pt or Au electrodes, with dendritic structure in the surface layers of the polymer backbone).

Both these models were derived based on the PDEs of the governing physical processes within the sensor and actuator while taking into account the surface resistance effects. The resulting infinite-dimensional Laplace domain models were further reduced to lower-order models in the form of rational transfer functions usable for real-time computation and control design. In the following we introduce the adaption of these models to describe sensing and actuation dynamics of our IEAP sensor–actuator, and their use for control design. Construction of the resulting models is illustrated in figure 4. For clarity, the notations are adapted from [23, 45] where possible.

2.3.1. Modelling the sensor dynamics. The model of IEAP sensing adapted from equation (55) in [45] relates the out-of-plane displacement of the tip of the IEAP beam $w(s)$ to the short-circuit current between the material electrodes $i(s)$, s being the Laplace variable. Assuming small deformations and sensor bending in the first cantilever shape mode (using the spatial derivative of the 1st cantilever shape mode in the tip of the beam), the relation between $w(s)$ and the manipulator tip position $x(s)$ can be expressed as a constant $C = L/(1.3765L_e + L)$, where L is the length of the IEAP and L_e is the length of the elongation from the IEAP to the measuring plane. The sensing model can be written as:

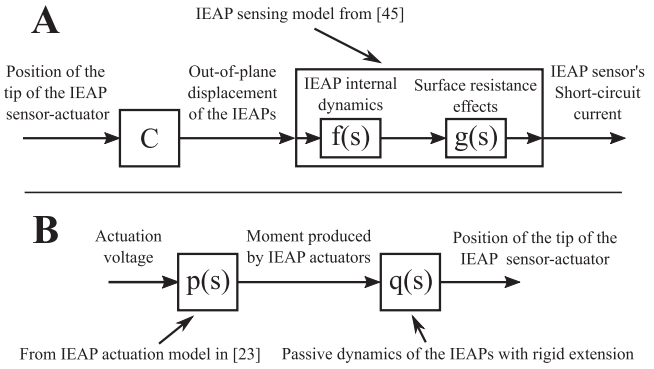

Figure 4. Block diagrams describing the construction of the IEAP (A) sensing and (B) actuation models.

$$\hat{H}(s) = \frac{i(s)}{x(s)} = C \cdot f(s) \cdot g(s), \tag{1}$$

with $f(s)$ describing the sensing dynamics and $g(s)$ incorporating the surface resistance effects (see figure 4(A)). These parts can be re-written in a practical form for application:

$$f(s) = \frac{\lambda_1 s^3 + \lambda_2 s^2 + \lambda_3 s}{s + K}, \tag{2}$$

$$g(s) = \frac{\mu_1 s^2 + \mu_2 s + \mu_3}{s^2 + \mu_4 s + \mu_5}, \tag{3}$$

with the terms in $f(s)$:

$$K \approx \frac{F^2 d C^-}{\kappa_e R T}, \tag{4}$$

$$\lambda_1 = -\frac{3YW_s h\sqrt{Kd}}{8\alpha_0 L^3 K^2}; \qquad \lambda_2 = -4K\lambda_1,$$
$$\lambda_3 = 8K^2\left(\sqrt{\frac{d}{h^2 K}} - 1\right)\lambda_1, \tag{5}$$

and in $g(s)$:

$$\mu_1 = \frac{L^2}{6}, \qquad \mu_2 = \frac{3h}{\kappa_e r_0}, \qquad \mu_3 = \frac{12h^2}{\kappa_e^2 r_0^2 L^2},$$
$$\mu_4 = \frac{12h}{\kappa_e r_0 L^2}, \qquad \mu_5 = \frac{24h^2}{\kappa_e^2 r_0^2 L^4}. \tag{6}$$

As in [23, 45], the terms are: Y is the Young's modulus, W_s is the width of the IEAP sensor, d is the ion diffusivity, h is the half the material thickness, α_0 is the charge–stress coupling constant, κ_e is the dielectric permittivity, r_0 is the surface resistance per material length and width, F is the Faraday constant, C^- is the anion concentration, R is the universal gas constant, and T is the absolute temperature. For more details about the model, refer to [45].

The resulting model is improper as its numerator is of higher order than the denominator; however, in the experiments we use its proper inverse.

2.3.2. Modelling the actuation dynamics. The model for actuation dynamics is adapted from the work of Chen *et al* [23]. They linked the bending dynamics of a long flexible IPMC beam to the input voltage by deriving the model for voltage-induced bending and cascading it with the second-order vibration dynamics of a flexible beam. In this work we model the actuation dynamics of the IEAP sensor–actuator considering the system as a rigid beam with non-uniform cross-section that is connected to the Earth frame by a pivot joint (IEAPs) with torsional stiffness. The joint is actuated by torques generated by the IEAP actuators, where the model relating the IEAP input voltage to the bending moment is adapted from the intermediate results of Chen *et al* [23]. Naturally, we split the actuation dynamics into two parts—the actuation model $p(s)$ relating the produced moment $M(s)$ to the applied voltage $V(s)$, and the mechanical model of the device's passive dynamics $q(s)$ relating the input moment $M(s)$ to the position $X(s)$ of the tip of the rigid link attached in the mobile end of the IEAP sensor–actuator (see figure 4(B)):

$$G(s) = \frac{X(s)}{V(s)} = p(s) \cdot q(s). \tag{7}$$

We assume that the surface resistance along the IEAP actuator's electrodes is zero ($r_1' = 0$) as the actuator is very short, and the surface resistances of the materials in hand are low. With some manipulations one can extract the expression for $p(s)$ from the intermediate results (particularly, equations (20), (29) and (46)) in [23]:

$$p(s) = \frac{M(s)}{V(s)} = \frac{\alpha_0 \kappa_e K W_a h (1-\gamma)}{\gamma \kappa_e r_2' s^2 + \gamma (h + \kappa_e K r_2') s + K h}, \tag{8}$$

where K is given in equation (4) and γ is defined as:

$$\gamma = h\sqrt{\frac{K}{d}}, \tag{9}$$

r_2' is the resistance through the IEAP per length and W_a denotes the width of the actuator. It must be noted that when neglecting the surface resistance, the actuation moment does not depend on the IEAP length.

The passive dynamics of the rigid mobile link attached to the IEAPs can be captured with a second-order system

$$q(s) = \frac{X(s)}{M(s)} = \frac{\mathcal{L}}{I} \cdot \frac{1}{s^2 + 2\xi\omega_n s + w_n^2}, \tag{10}$$

which is valid for the frequency range of interest. Here I is the moment of inertia with respect to the clamping axis, ξ accommodates the damping of the environment and internal friction in IEAPs, ω_n is the natural frequency of the system and $\mathcal{L}$ is the distance from the IEAP clamping level to the position-measuring height on the mobile link.

2.3.3. Control. Based on the model for actuation dynamics we design two controllers, a PI controller and an H_∞ controller. The PI controller is manually tuned to achieve shortest settling time in tracking a step input.

The H_∞ controller is designed according to the procedures given in [48]. The sensitivity weight on output error W_e (low-pass) and the weight on control effort W_u (high-pass) were used in the design procedure according to [48, 49]. First- and second-order weights are used to design the controller that is later reduced to the fifth order for implementation purposes.

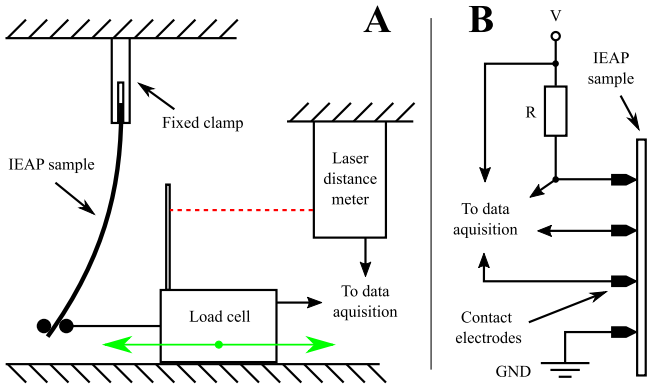

Figure 5. Experimental setups for measuring the material's (A) Young's modulus and (B) dimension-normalized surface resistance.

2.4. Experimental setups

The experimental setup used to measure Young's modulus is illustrated in figure 5. The material sample is suspended in air using a fixed clamp. The tip of the sample is held between a fork attached to a force gauge Panlab TRI202P and its position is measured using a laser distance meter SICK OD2-P250W150U0. The force and position readings are recorded using a PC computer with NI PCIe-6343 data acquisition board and NI Labview 2010 environment. The force gauge position is changed manually and its position is fixed at the instances of recording the readings.

The four-point resistance measurement setup used to determine the material's surface resistance is illustrated in figure 5. The material sample is pressed against the electrodes and a constant voltage of 0.1 V is applied. The voltages on the resistor and on the inner electrodes are measured and the surface resistance per length and width r_0 is calculated using the same PC computer with NI PCIe-6343 and NI Labview 2010.

The diagram of the setup used in the rest of the experiments is shown in figure 6 and a photo of the actual setup is in figure 7. The spring-loaded clamp is fixed such that the mobile link of the IEAP sensor–actuator is hanging down, since in such a configuration the gravity does not cause any lateral strains in the IEAPs in the rest position. In the spring-loaded clamp, the actuators are electrically connected in parallel to each other. They are driven from a PC through the amplifier of a Kepco BOP 20-10MC bipolar power supply that is optimized for capacitive loads. The sensor's short-circuit current is measured using a two-stage amplifier (based on OPA111BM operational amplifiers), that converts the

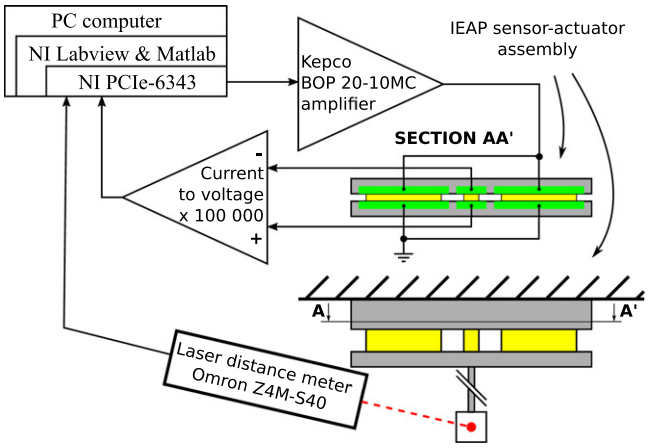

Figure 6. Experimental setup that is used to measure the damping ratio, natural frequency and frequency responses in the model identification phase, and to perform the feedback experiments.

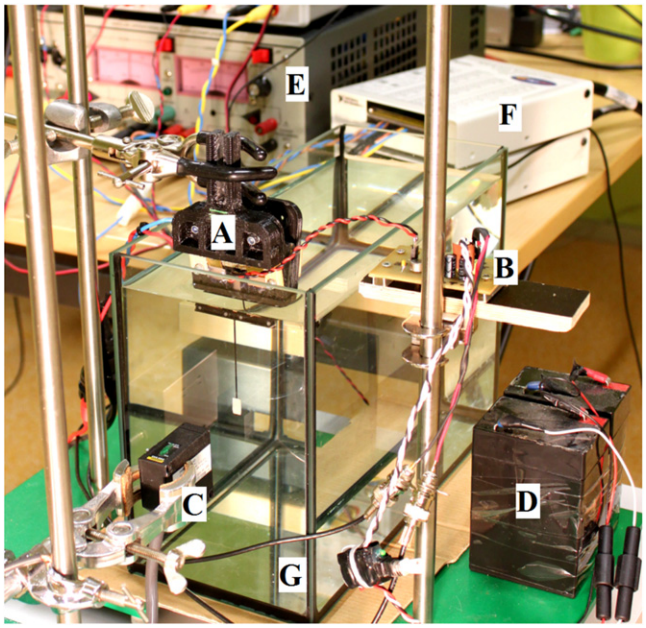

Figure 7. A photo of the final experimental setup used in feedback experiments and in some system identification experiments. (A) The proof-of-concept IEAP sensor–actuator; (B) short-circuit current-to-voltage converter and amplifier; (C) laser distance meter; (D) amplifier's battery pack; (E) power supply unit Kepco; (F) data acquisition board's terminal boxes; (G) water tank (only used with the samples that must be kept hydrated, currently set #3).

current to voltage and amplifies the signal (by factor of 100 000). The amplifier's power is supplied from a battery pack to eliminate noise propagation from the power grid. The position of the tip of the mobile link is measured using an Omron Z4M-S40 laser distance meter with resolution of 40 μm. The experiments are controlled from a PC computer with NI Labview 2010 SP1 software through NI PCIe-6343 data acquisition board. Program loops in frequency response measurements and feedback control experiments are implemented with a sampling frequency of 10 kHz.

2.5. Parameter identification

The terms in the sensing and actuation models (sections 2.3.1 and 2.3.2) include known constants (universal gas constant R and Faraday's constant F) and parameters that must be identified for each material prior to the control design and closed-loop control experiments.

First, the average material thickness $2h$ and the surface density of the material sheet are determined. Young's modulus Y of the sheet is identified from the bending experiments of the material beam, i.e. deformations are applied and the corresponding forces are measured at the tip of the vertically suspended material sample (see the setup in figure 5(A)). The ratio between the applied forces P and the resulting deformations σ is determined using linear regression, and Young's modulus is obtained according to [50]:

$$Y = \frac{Pl^3}{3\sigma I_y}, \quad I_y = \frac{(2h)^3 w}{12}, \tag{11}$$

where l is the length of the material sheet, I_y is the area moment of inertia, and w is the width of the material sample. The dimension-normalized surface resistance r_0 is obtained using a four-point resistance measuring scheme (0.1 V applied, measurements taken in steady state) shown in figure 5(B).

Next, the sample sets (two actuators, one sensor) are cut from the respective material sheet targeting widths of 3 mm and 10 mm for the sensor and actuators respectively. The sensor–actuator prototype is assembled and the width of the sensor W_s, widths of the actuators W_a and the length of the IEAPs L are measured. The moment of inertia for the assembly of the IEAPs and the mobile link is calculated (with respect to the outer clamping edge of the fixing clamp) from their geometry and the densities of their parts. The sensor–actuator device assembly is suspended vertically and the laser distance meter is set to point the tip of the extension rod. The effective length of the actuating portion L_e (from the clamp to the laser distance meter level) is measured.

Once the setup is complete, the natural frequency w_n and the damping ratio ξ are determined from free oscillations (due to external stimulus) of the mobile link. Next, the frequency responses are measured for actuation and sensing dynamics. Sinusoidal voltage inputs of 2 V amplitude are sequentially applied on the actuators, with frequencies logarithmically spaced in the 0.2–15 Hz, or wider interval (aiming to capture the characteristic phase transitions), for the duration of at least two full periods, but no less than 30 s. Simultaneously, the position of the tip of the link and the IEAP short-circuit current are measured using a laser distance meter and a current amplifier, respectively. The magnitude and phase information is extracted, and transfer function models for actuation and sensing dynamics are then identified through curve-fitting the remaining model parameters that cannot be determined individually (i.e., ion-diffusivity d, charge–stress coupling constant α_0, dielectric permittivity κ_e, anion concentration C^-, and resistance trough the polymer r_2').

While curve-fitting cannot uniquely define all these parameters, the structure of the models (in chapters 2.3.1 and

Table 1. Identified model parameters for each IEAP sensor–actuator assembly.

Measured or calculated parameter	Symbol	# 1	# 2	# 3	Unit
Material thickness	$2h$	277	353	282	μm
Young's modulus	Y	140	154	658	MPa
Surface resistance	r_0	0.543	64.0	0.144	Ω
Total width of the actuators	W_a	18.9	20.8	20.8	mm
Sensor width	W_s	1.95	3.72	2.96	mm
Operational material length	L	3.03	2.53	2.22	mm
Effective length of elongation	L_e	61.0	59.64	58.60	mm
Moment of inertia about clamp	I_{xx}	1.79×10^{-7}	1.71×10^{-7}	1.66×10^{-7}	kg m^2
Material surface density	ρ	0.460	0.650	0.570	kg m^{-2}
Natural frequency	ω_0	15.9	8.70	10.0	Hz
Damping ratio	ξ	0.0611	0.100	0.135	—
Room temperature	t	22.4	22.9	21.6	°C
Fitted parameter					
Ionic diffusivity	d	3.44×10^{-12}	3.48×10^{-11}	3.32×10^{-11}	m^2 s^{-1}
Anion concentration	C^-	1064	1068	1089	mol m^{-3}
Resistance trough material	r_2'	9.98×10^{-6}	9.99×10^{-6}	1.00×10^{-5}	Ω m
Dielectric permittivity for sensor	κ_{e_s}	3.76×10^{-3}	1.52×10^{-3}	1.38×10^{-3}	F m^{-1}
Dielectric permittivity for actuator	κ_{e_a}	2.99×10^{-6}	5.07×10^{-7}	1.41×10^{-7}	F m^{-1}
Charge–stress coupling constant for sensor	α_{0_s}	1.39×10^5	3.35×10^5	3.18×10^5	J C^{-1}
Charge–stress coupling constant for actuator	α_{0_a}	−0.213	−0.0220	−0.0828	J C^{-1}

2.3.2) offers certain constraints, and when approximate numbers for initial values are chosen according to the literature [23, 44, 45, 51], the fitting process converges to real-valued physically realistic parameters. Initial values for anion concentration C^- and ion diffusivity d are chosen according to [44] (except for d in case of material #1, that is taken from [51]), while the rest of the parameters are taken from the results in [23, 45]. Curve-fitting these parameters is performed in Matlab environment, where we apply unconstrained nonlinear optimization (*fminsearch* function) in order to minimize the cost function that accounts for the errors between the measured frequency responses and the model predictions, both in sensing and actuation dynamics.

After the models for both the actuation and sensing dynamics are identified, we proceed with the experiments to characterize the performance of the closed-loop system.

2.6. Performance characterization

The performance is characterized in the following four types of experiments: step response, sinusoidal reference following at four different frequencies, random reference following at three different spectra, and finally long-duration sinusoidal reference following for testing of the stability.

The results are compared to determine the dependency of performance on material type and control scheme (particularly whether robust control is essential), and to investigate the differences between the IEAP sensor feedback performance against the laser distance sensor-based external feedback.

3. Experimental results

The material and system parameters were measured or curve-fitted as described in section 2.5 and the resulting parameters for all sample sets are summarized in table 1. The measured and fitted frequency responses for sensing and actuation dynamics are shown in figures 8 and 9 respectively.

Based on the actuator models, an H_∞ and a PI controller are designed, as described in section 2.3.3. Next, the step responses of the closed-loop systems are measured using the reference signal $u(t) = U(t - 0.5s)$ mm, where $U(\cdot)$ is the Heaviside step function. Each of the experiments' duration is 15 s. Tracking errors (i.e. difference between the reference and the actual position) measured by the laser distance sensor are shown in figure 10 and the step responses are characterized quantitatively (delay time t_d to reach 50% of the reference, rise time t_r from 10% to 90%, peak time t_p, percent overshoot PO and settling time t_s for 5% bound) in table 2.

The dry sample set (#1) exhibits strong high-frequency noise (up to 20% of the reference position) in the position estimation (caused by high gain in the high frequency range in the sensor's inverse model). Thus, before extracting the figures from the experimental results for this sample set in IEAP feedback configuration, we apply down-sampling by ten times.

Sample set #3 shows strong nonlinear behaviour both in sensing and actuation. Out of all used materials, it exhibits the strongest low-frequency drift in short-circuit sensing current, causing erroneous position estimation. Also, the actuator is unable to keep reference position for the duration of the experiment even in the laser feedback configuration (voltage remains in saturation after 5.627 s for PI/laser, 2.354 s for PI/

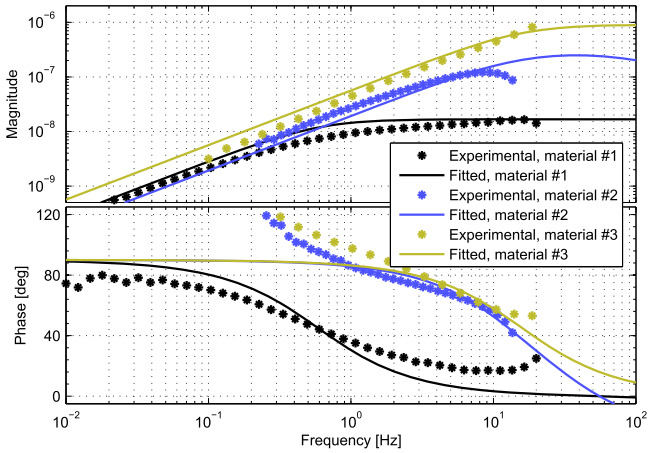

Figure 8. Measured and fitted frequency responses relating the short-circuit current of the IEAP sensor to the position of the tip of the rigid link. Measured frequency interval is varied to capture the phase transition in sensing dynamics.

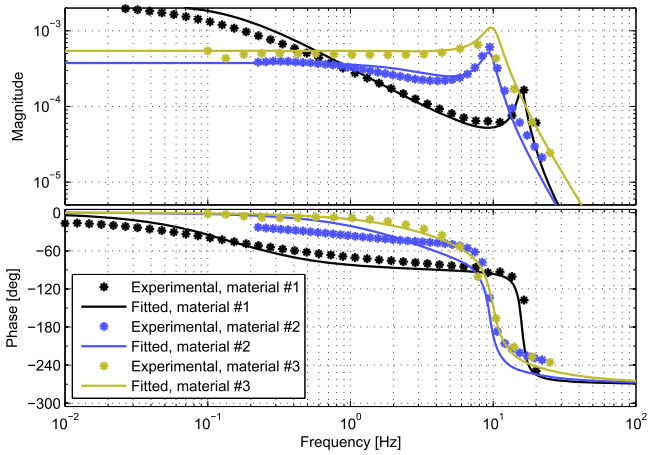

Figure 9. Measured and fitted frequency responses relating the position of the tip of the rigid link to the voltage applied to the IEAP actuators.

IPMC, 11.291 s for H_∞/laser and 1.550 s for H_∞/IPMC feedback configurations). The control voltage reaches saturation at the 3.5 V limit, reference is not followed and eventually material bends backwards beyond its resting position. Experiment is halted to protect the actuators. In PI/laser configuration the sample set #3 fails to stabilize to 5% bound and its settling time is shown for 10% bound.

For comparison, the step responses of the identified actuation models in closed-loop configuration with the designed PI and H_∞ controllers are simulated using Matlab R2015b software. The results are shown in figure 11, and characterized in table 3.

Sinusoid tracking experiments are performed at four frequencies, i.e., 0.5, 1, 2, and 3 Hz. Each experiment duration is 30 s unless the control voltage saturates and it has to be aborted to prevent damaging the materials. One way to characterize these results is through the difference in the magnitude and phase between the reference and laser distance

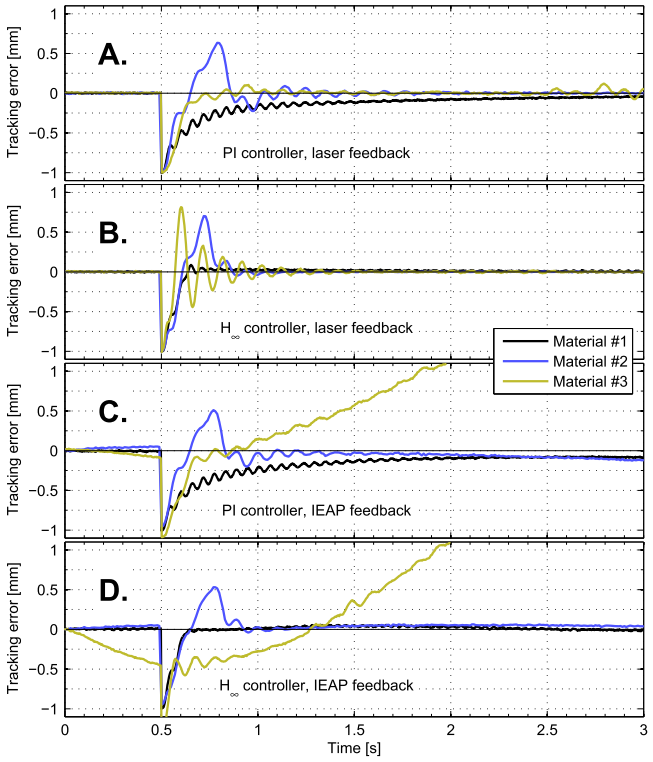

Figure 10. Tracking errors for the experimentally measured step responses. First 3 s of the experiments are shown.

meter readings (at the reference signal frequency), and through the RMS error over the course of the experiment. These results are given in table 4. The magnitude and phase differences are extracted using Fourier transform while the RMS error is calculated in the time domain. The evolution of the RMS errors over each period during the experiments is shown in figure 12. The reference and the laser distance meter readings during the experiments over a single period are shown in figure 13 for illustrative purposes. The displayed period begins at 2 s after the start of the experiment.

In the random reference tracking experiments the same set of input signals is applied to all the sample sets. The signals are generated using sequences of random numbers passed trough a fourth-order Bessel bandpass filter (at 10 kHz sampling rate). Three frequency intervals are used, with lower frequency 0.1 Hz and the upper frequency of either 2, 3 or 4 Hz. The duration of the experiments is 30 s. The results for various configurations are characterized by the RMS tracking error over the whole experiment duration in table 5. Some experiments (marked in the table) are halted before they reached 30 s to prevent damaging the materials. As these numbers alone give too little details, we further plot the RMS error over each 0.5 s of the experiment in figure 14, and the first 2 s of the experiment course in figure 15.

The extended sine tracking experiments are conducted using only the H_∞ controller, first with IEAP feedback and then with the laser feedback. The reference signal is a 1 Hz sine wave with 1 mm amplitude that is applied for 30 min and 2 h for the IEAP and laser feedback, respectively, unless the

Table 2. Characterization of the experimentally measured step responses.

Feedback		#	$t_d(s)$	t_r (s)	$t_p(s)$	PO (%)	$t_s(s)$
PI	Laser	# 1	0.096	1.066	4.762[a]	1.52%	2.440
		# 2	0.060	0.120	0.290	63.4%	0.800
		# 3	0.087	0.132	0.221	12.4%	2.500[b]
	IEAP	# 1	0.144	1.164	—[a]	—	—
		# 2	0.060	0.120	0.270	51.1%	—
		# 3	0.114	0.127	0.280	216%	—[b]
H_∞	Laser	# 1	0.074	0.096	0.154	8.82%	0.212
		# 2	0.080	0.080	0.220	70.2%	0.350
		# 3	0.054	0.052	0.099	83.3%	0.768[b]
	IEAP	# 1	0.072	0.088	0.192	5.79%	0.781
		# 2	0.080	0.110	0.270	53.0%	0.914[2]
		# 3	0.057	0.667	0.990	195%	—[b]

[a] Overdamped system.
[b] Following the reference failed before intended end.

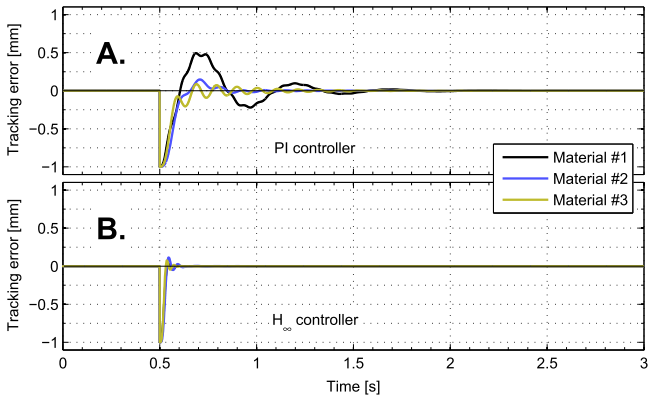

Figure 11. Tracking errors in the simulated step responses for the identified actuation models in closed-loop configuration with the respective (A) PI and (B) H_∞ controllers.

Table 3. Characterization of the simulated step responses for the identified actuation models in closed-loop configuration with the designed PI and H_∞ controllers.

Feedback	#	$t_d(s)$	$t_r(s)$	$t_p(s)$	PO(%)	$t_s(s)$
PI	# 1	0.053	0.074	0.188	49.4%	0.781
	# 2	0.070	0.073	0.201	14.7%	0.252
	# 3	0.054	0.055	0.190	8.74%	0.404
H_∞	# 1	0.023	0.021	0.045	3.07%	0.036
	# 2	0.026	0.019	0.047	11.5%	0.071
	# 3	0.021	0.016	0.037	7.59%	0.042

control voltage saturates for an entire reference signal period. The results are characterized by the RMS error over each reference signal period shown in figure 16. In table 6 the duration of each experiment is given. For sample set #2 in laser feedback configuration the experiment is halted due to external disturbance. During these experiments we also measure the actuation current and calculate the period-averaged power consumption that is given in figure 17.

4. Discussion

A prototype of the IEAP sensor–actuator utilizing the same type of materials for sensing and actuation within the same device is built and characterized in this work.

When designing the experiments we intended to obtain consistent fits between the sensing and actuation dynamics in terms of parameters describing the material properties. Naturally, the charge–stress coupling constant α_0 remains different as it results from distinct processes in sensing and actuation context. The only parameter that does not match is the dielectric permittivity κ_e while the rest are the same for sensing and actuation dynamics. We speculate that there exist unidentified processes in sensing and/or actuation mechanisms of the CPCs and IPMCs that have not been accounted for.

While comparing the experimentally measured frequency responses to the identified models in figures 8 and 9, the discrepancies clearly indicate that both for actuation and sensing there exist some unmodeled dynamics. This does not disturb remarkably the control design and feedback experiments, and in fact, is completely expected, considering the relatively complex derivation process of the physics-based control-oriented models in [23, 45]. Feedback configuration well compensates for the inaccuracies in the actuation model while the discrepancies in the sensing model cause small systematic errors both in phase and magnitude in the IEAP feedback experiments. One possibility to improve the modelling accuracy is to further extend the modelling scope of the used physics-based models. Another, less laborious alternative is replacing the physics-based models with some 'grey-box' or 'black-box' models. In this work we avoided this approach as it gives only little or no information about the IEAP fundamental physical parameters.

The resulting sensors' unrealistic dielectric permittivities (under realistic constraints fitting does not converge) seem to suggest that it is not correct to presume that the entire thickness of the IEAP behaves as a dielectric medium. Thus, the resulting dielectric permittivities actually describe effective parameters of a parallel-plate capacitor with the

Table 4. Characterization of the experimental results of the closed-loop sinusoidal reference tracking.

	Control configuration	PI						H_∞					
		Laser			IEAP			Laser			IEAP		
	Material #	# 1	# 2	# 3	# 1	# 2	# 3	# 1	# 2	# 3	# 1	# 2	# 3
0.5 Hz	Amplitude (% of ref)	74.8	105	102	66.9	94.9	200	98.5	103	100	89.5	90.5	112
	Phase wrt ref (deg)	−22.8	−1.90	−13.6	−23.1	−0.986	−75.2	−3.75	−1.46	−2.94	−6.29	−0.881	−10.4
	RMS error (%)	30.5	4.64	15.4	35.3	106	380	4.87	2.94	4.51	29.3	99.3	143
1 Hz	Amplitude (% of ref)	64.5	113	101	58.7	106	22.7	98.0	108	101	89.9	103	72.8
	Phase wrt ref (deg)	−35.6	−4.70	−22.2	−33.5	−3.48	−92.0	−6.20	−4.45	−7.13	−8.07	−3.92	−3.89
	RMS error (%)	42.7	12.3	26.9	43.9	15.3	226	7.71	8.57	8.81	84.7	39.9	212
2 Hz	Amplitude (% of ref)	49.3	166	80.6	48.6	124	80.0	99.4	115	98.9	83.9	114	108
	Phase wrt ref (deg)	−51.2	−105	−47.8	−51.8	−84.7	−35.8	−10.7	−12.3	−13.2	−13.4	−14.9	−33.8
	RMS error (%)	55.4	155	52.8	95.9	211	112	13.5	19.6	18.3	226	59.8	59.8
3 Hz	Amplitude (% of ref)	37.8	125	61.9	36.4	121	66.6	87.4	117	97.4	67.3	112	64.0
	Phase wrt ref (deg)	−58.3	−120	−65.9	−57.0	−110	−88.7	−14.1	−27.6	−24.6	−33.1	−45.8	−76.6
	RMS error (%)	61.5	141	66.2	134	136	162	26.6	41.1	30.4	386	67.3	191

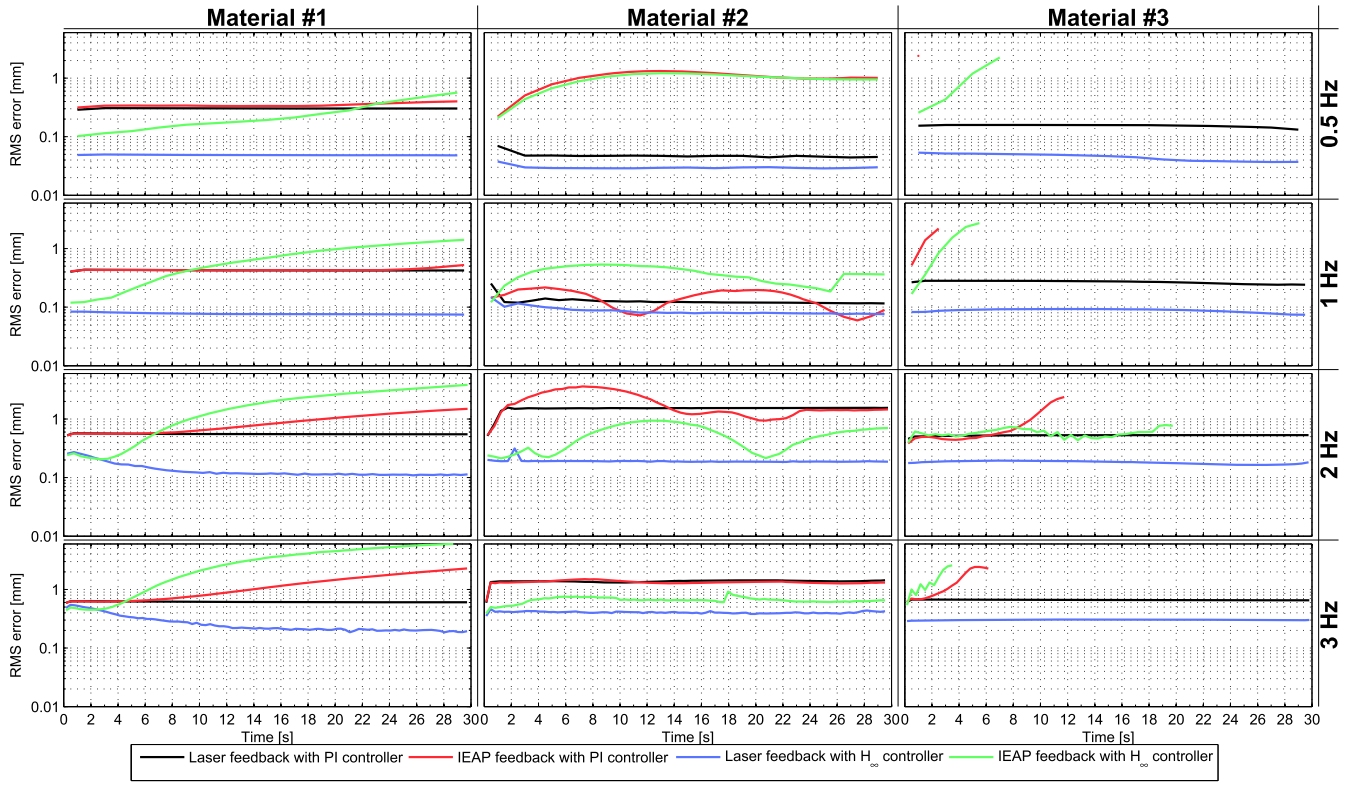

Figure 12. RMS errors in experimentally measured sinusoidal reference tracking. Calculated over each period of the sinusoidal reference signal.

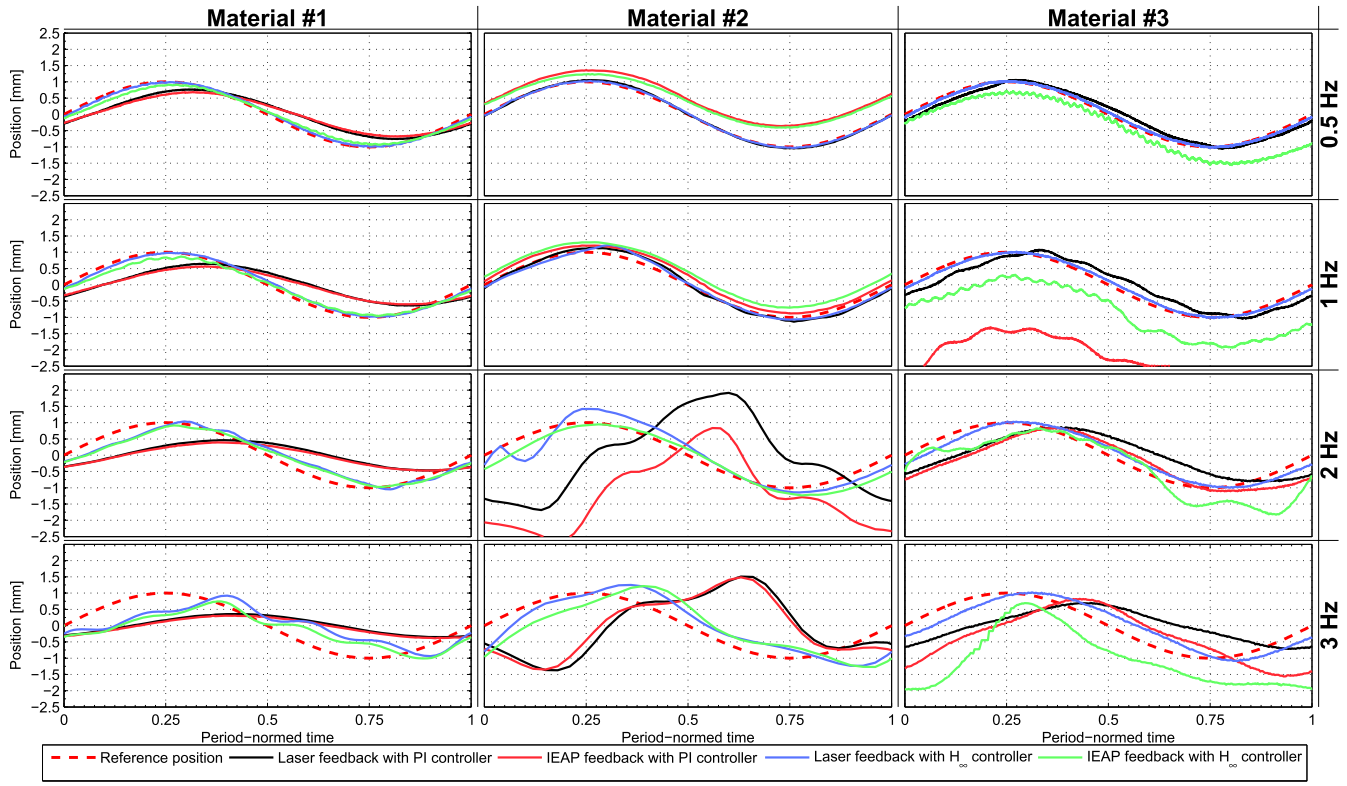

Figure 13. Reference signals and experimentally measured positions in sinusoidal reference tracking experiments. Single period is plotted for each experiment, starting at 2 s from the beginning of the experiment.

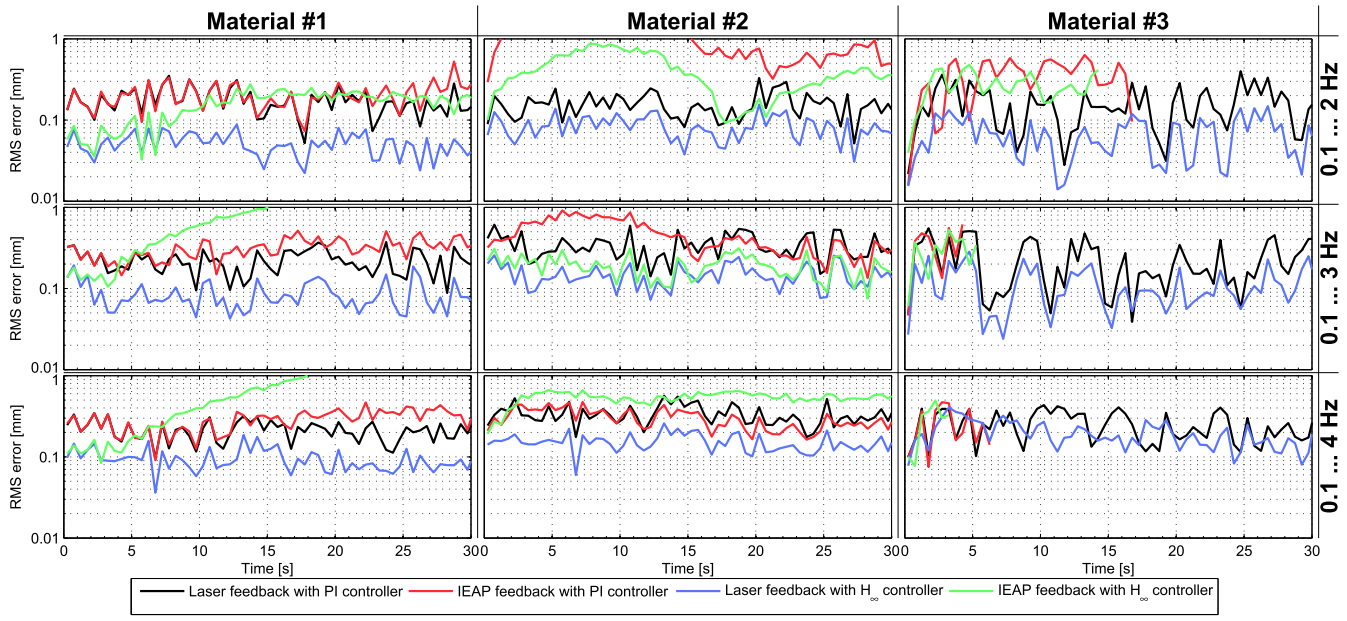

Figure 14. RMS error in random reference following experiments. Calculated over each 0.5 s interval.

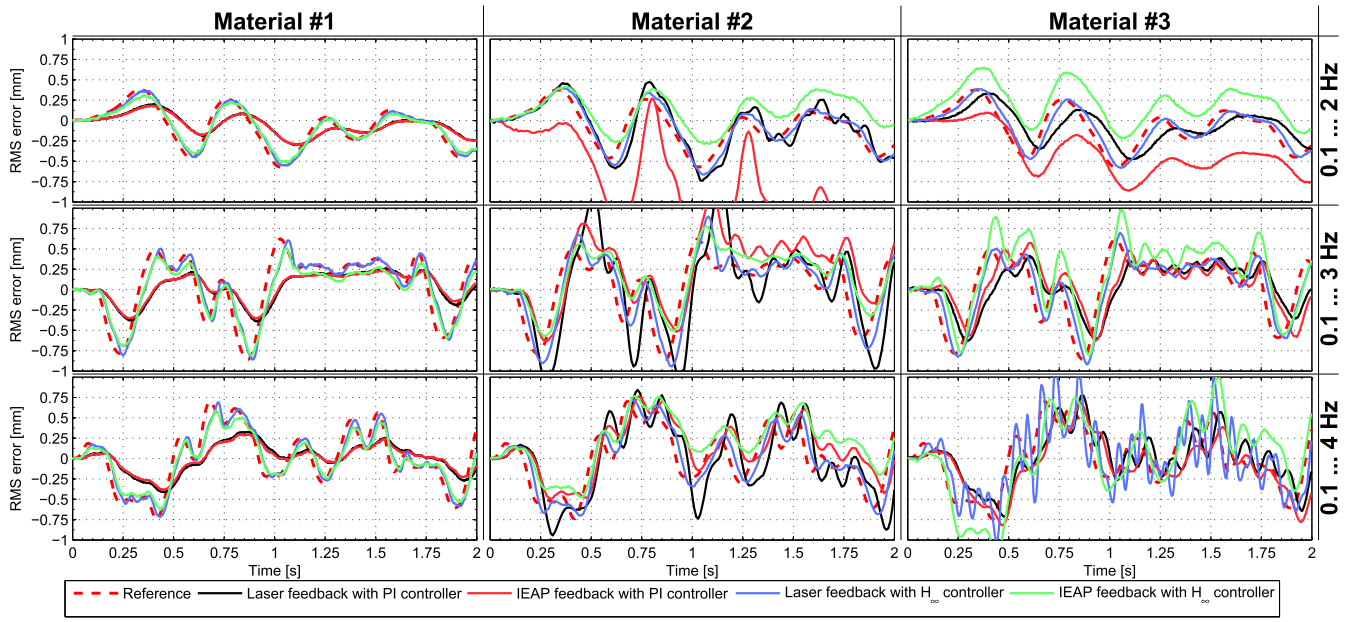

Figure 15. Reference signal and measured position in the random reference following experiments. First 2 s of the experiments are plotted.

Table 5. RMS errors (mm) in random reference following experiments.

Control config.	PI						H_∞					
	Laser			IEAP			Laser			IEAP		
Material #	# 1	# 2	# 3	# 1	# 2	# 3	# 1	# 2	# 3	# 1	# 2	# 3
0.1–2 Hz interval	0.190	0.167	0.189	0.219	1.32	0.637[1]	0.0541	0.0884	0.0793	0.170	0.470	1.08[2]
0.1–3 Hz interval	0.233	0.363	0.257	0.327	0.507	1.06[3]	0.0930	0.156	0.127	1.19	0.201	1.78[4]
0.1–4 Hz interval	0.223	0.348	0.251	0.297	0.309	1.90[5]	0.0986	0.156	0.165	0.989	0.543	1.46[6]

Note: Marked experiments were aborted at [1]17.0*s*, [2] 14.7*s*, [3]4.56*s*, [4]5.82*s*, [5]6.88*s* and [6]3.90*s* to prevent harming materials with saturated driving voltage.

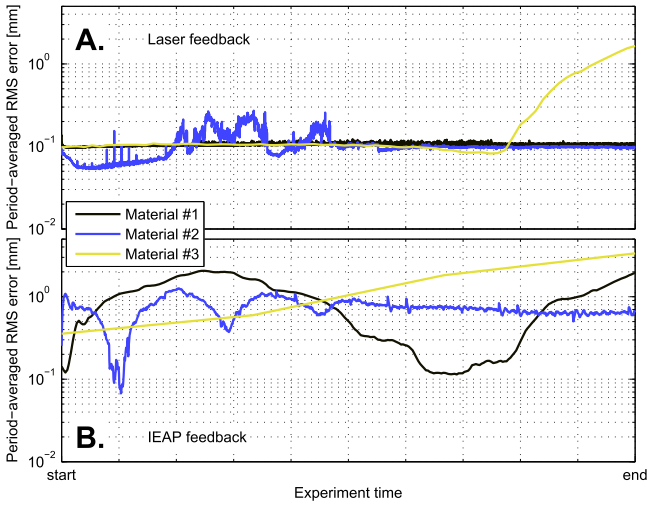

Figure 16. RMS error over each period in the long-term sinusoidal reference following. (A) Laser feedback; (B) IEAP feedback. Time is normalized to the experiments' durations for plotting purposes. Durations are given in table 6.

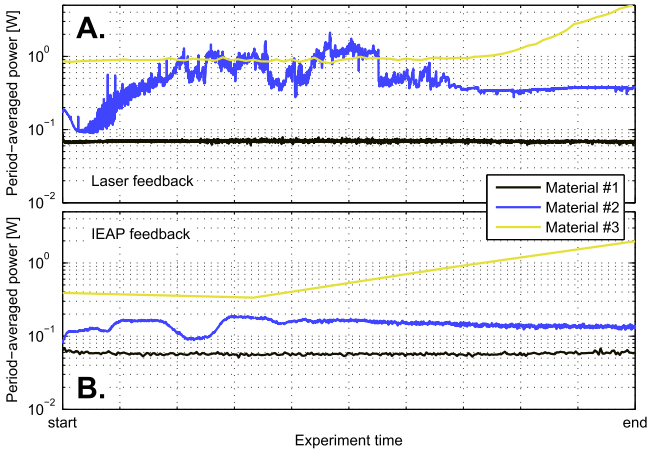

Figure 17. Power consumption of the IEAP actuators in long-term sinusoidal reference following experiments. (A) shows the results for laser feedback, (B) for IEAP feedback. Time is normalized to the experiments' durations for plotting purposes. Durations are shown in table 6.

dimensions of the IEAP. In fact, the effective thickness of a parallel-plate capacitor with the surface area of the IEAP has later been shown to be (approximately) equal to the depth of the counter-ion boundary layers near the IEAP electrodes (see [52]). Despite the described inaccuracies, the models in hand are the best set of control-oriented physics-based models available at the time and they well approximate the measured frequency responses of the sensing and actuation dynamics.

Comparing the closed-loop step response simulation predictions (figure 11 and table 3) to the experimental results (figure 10 and table 2) shows that the actual performance of the sensor–actuator device is inferior to the predictions. Resulting settling times and other figures are in experimental results multiple times larger (except the overshoot for the material #1 in laser feedback configuration with PI controller). That is because our simulation results characterize best scenario performances, i.e. when voltage saturation, external disturbances, model perturbations, noises of various origins, etc are not present. Properly addressing these processes is very laborious.

Examining the results reported in tables 2–6 and figures 10–16 allows to compare the IEAP feedback performance material-wise, controller-wise, and against external feedback. The main limiting factor in IEAP feedback concept appears to be the low-frequency drifting in the sensors' short-circuit current, that varies material-wise in magnitude, and respectively in impact on the performance. Its potential causes include interactions between the amplifier and the material, environmental influences, potential material degradation (see [53]) and internal dynamics effects, and needs further investigation.

Performance in closed-loop experiments with IEAP sensing remained inferior to the laser distance meter feedback due to the aforementioned low-frequency sensing noise. It degrades the system's long-term performance while in the short run (few seconds) they do not differ significantly (see figures 10, 12 and 14).

It is also seen in the experiments (see tables 2, 4 and 5) that the H_∞ controller performs better and should be preferred over the PI controller (including the step response which the PI is tuned for). This suggests that the complexity of the IEAP actuation dynamics can be compensated with proper model-based control, either using the physics-based 'white box' models that we use in this work, or some less complex 'grey-box' or 'black-box' models, e.g. fully empirical models used in our previous work [39].

While sample sets #1 and #2 perform similarly in all experiments, the set #3 performs much worse than the others. Its actuator's 'zero' position changes even under sinusoidal reference following (see laser feedback duration experiment in figure 16), eventually saturating the input voltage and failing to follow the reference. Also, its position sensing is very noisy, causing most of the experiments to be aborted soon after they begin. It is not clear what processes cause or dominate these unwanted effects. In terms of actuation, the shorter operational length of the sample set #3 does not seem to influence the actuation magnitude remarkably (see figure 9). Instead, we speculate that the nonlinear actuation behaviour is caused by the significantly higher material stiffness (table 1). According to [54], when the pressure within the cathode boundary layer clusters within the polymer backbone increases (stronger effect in stiffer materials), the additional cations near the cathode start extensive restructuring and redistribution, that is responsible for back-relaxation, and possibly also for our observations. In terms of sensing, sample set #3 has significantly larger charge–stress coupling constant than the other materials, and it exhibits stronger short-circuit current (see table 1 and figure 8), that the sensing model in chapter 2.3.1 also explains with higher Young's modulus. We hypothesize that mechanical stress in IEAPs drives some additional nonlinear ion and solvent dynamics that is responsible for the low-frequency sensing noise, and thus the noise is stronger in materials with higher Young's modulus.

Table 6. Experiment durations for long-term sinusoidal reference following.

Feedback	Laser			IPMC		
Material	#1	#2	#3	#1	#2	#3
Duration	7200 s	4513.3 s	76.82 s	300 s	1800 s	4.295 s

In long-term actuation experiments with IEAP feedback the sensing signal of the sample set #1 is less stable than in case of the set #2 (figure 16). This experiment is halted at 300 s to avoid damage to the actuators while the material #2 runs the entire 30 min experiment. Comparing to the longest IEAP feedback control experiments reported so far (20 s, [38]), it is 15 and 90 times longer respectively. In other experiments the drifting in the sensors' short-circuit sensing current varies material-wise, but between materials #1 and #2 clear superiority cannot be seen.

The actuation performances of these materials are also similar, but cannot be directly compared due to the difference in the environments. The external influences acting on the sample set #1 in the air are insignificant, while the set #2 in the water experiences also the added mass effects in addition to greater damping. In the long-term laser feedback experiments both materials work reliably for the entire experiment durations, i.e., over 1 h. The higher power consumption of the sample set #2 can be explained with the damping effects (figure 17), but the causes of its fluctuations are unclear (potentially a poor actuator contact). Among these two IEAPs (#1 and #2), it is primarily the working environment that should dictate which one to prefer.

In the feedback experiments our IEAP sensor–actuator performed well over 7500 and 4900 cycles with material #1 and #2 respectively, without noticeable signs of performance degradation. Thus, considering the typical properties and degradation [53] of the IEAP materials and feedback results presented in previous studies (see section 1), the proposed design is shown to work very well. The factors that could limit its applications are primarily associated with the material properties. Actuation-wise, larger achievable deformations could be desirable, and sensing-wise, the reason for low-frequency sensing noise should be identified and suppressed. The large amount of experiments conducted in this paper well address the strengths and weaknesses of the IEAPs and hopefully will aid in material selection for applications.

5. Conclusions

In this work we propose and test an IEAP sensor–actuator device with integrated actuation and sensing capability. The proposed pivot-like design allows to combine the benefits of both the 'smart' IEAP materials and the matured tools of conventional robotics. We describe the design concept and the prototype, introduce the physics-based control-oriented models of sensing and actuation dynamics, their identification procedures, the experiment courses and the performance evaluation metrics. Closed-loop experiments with the IEAP sensor–actuator prototype are performed, and the results are presented for three different IEAP materials, two controllers and two feedback sources.

The proposed design is proven to work well considering the rather nonlinear and unstable properties of the IEAP materials. The H_∞ control is shown to offer significant improvements over PI controller. Thus identifying the system using physics-based models as in this work, or with some less involved black- or grey-box models and designing a model-based controller is recommended. Position feedback from the laser distance meter expectedly results in more stable performance while the low-frequency noise in the sensors' short-circuit current limits the timespan of reliable position feedback from the IEAP sensing scheme. The cause of this noise is unknown and we intend to further investigate it in our future work.

Sample sets #1 and #2 perform similarly and a particular material should be preferred depending on the work environment (air or water, respectively). The different environment is also the reason why these materials cannot be compared in more detail. Sample set #3 performs significantly worse than the others, exhibiting strong nonlinear relation between input voltage and output position for the actuators and very strong low-frequency noise in short-circuit current for the sensor.

In feedback experiments the sample sets #1 and #2 performed in total well over 7500 and 4900 sinusoidal cycles respectively, material #3 was able to perform less than 450 cycles. In laser distance meter feedback configuration we did not see signs of performance degradation even at the end of 2 h long experiment, and in IEAP sensor feedback configuration we were able to conduct 30 min long sinusoidal reference following without saturating the actuation voltage. In IEAP feedback configuration this is 90 times longer experiment than achieved in previous reports.

With all the presented results the proposed sensor–actuator realization is thoroughly characterized, making it also a good basis for choosing the control and feedback scheme, and the materials to work with in the applications for those not familiar with the IEAP materials.

Acknowledgments

Authors thank Andres Punning and Urmas Johanson (IMS Lab, University of Tartu) for providing materials and their constructive support during this work. This work was supported by US CRDF Grant No. 16059 and Estonian Research Council Projects SF0140018s12 and IUT33-9.

References

[1] Bar-Cohen Y 2004 Turning heads *IEEE Spectr.* **41** 28–33

[2] Shahinpoor M and Kwang J K 2001 Ionic polymer-metal composites: I. Fundamentals *Smart Mater. Struct.* **10** 819–33

[3] Palmre V, Brandell D, Mäeorg U, Torop J, Volobujeva O, Punning A, Johanson U, Kruusmaa M and Aabloo A 2009 Nanoporous carbon-based electrodes for high strain ionomeric bending actuators *Smart Mater. Struct.* **18** 095028

[4] Oguro K, Kawami Y and Takenaka H 1992 Bending of an ion-conducting polymer film-electrode composite by an electric stimulus at low voltage *J. Micromachine Soc.* **5** 27–30

[5] Palmre V, Brandell D, Mäeorg U, Torop J, Volobujeva O, Punning A, Johanson U and Aabloo A 2010 Ionic polymer metal composites with nanoporous carbon electrodes *Proc. SPIE* **7642** 76421D

[6] Shahinpoor M 1994 Continuum electromechanics of ionic polymeric gels as artificial muscles for robotic applications *Smart Mater. Struct.* **3** 367

[7] Guo S, Fukuda T and Asaka K 2003 A new type of fish-like underwater microrobot *IEEE/ASME Trans. Mechatronics* **8** 136–41

[8] Chen Z, Shatara S and Tan X 2010 Modeling of biomimetic robotic fish propelled by an ionic polymer-metal composite caudal fin *IEEE/ASME Trans. Mechatronics* **15** 448–59

[9] Punning A, Anton M, Kruusmaa M and Aabloo A 2004 A biologically inspired ray-like underwater robot with electroactive polymer pectoral fins *IEEE International Conference on Mechatronics and Robotics* **2004** 241–5

[10] Keshavarzi A, Shahinpoor M, Kwang J K and Lantz J 1999 Blood pressure, pulse rate, and rhythm measurement using ionic polymer-metal composite sensors *Proc. SPIE* **3669** 369–76

[11] Chen Z, Shen Y, Xi N and Tan X 2007 Integrated sensing for ionic polymer-metal composite actuators using PVDF thin films *Smart Mater. Struct.* **16** S262–71

[12] Kruusmaa M, Hunt A, Punning A, Anton M and Aabloo A 2008 A linked manipulator with ion-polymer metal composite (IPMC) joints for soft- and micromanipulation *IEEE Int. Conf. on Robotics and Automation* (Piscataway, NJ: IEEE) pp 3588–3593

[13] Ando B, Baglio S, Beninato A, Graziani S, Pagano F and Umana E 2012 A seismic sensor based on IPMC combined with ferrofluids *IEEE International Conference on Instrumentation and Measurement Technology (I2MTC)* pp 1829–32

[14] Abdulsadda A T and Tan X 2013 Nonlinear estimation-based dipole source localization for artificial lateral line systems *Bioinspiration Biomimetics* **8** 026005

[15] Shahinpoor M 2003 Ionic polymer-conductor composites as biomimetic sensors, robotic actuators and artificial muscles —a review *Electrochim. Acta* **48** 2343–53

[16] Pugal D, Jung K, Aabloo A and Kim K J 2010 Ionic polymer-metal composite mechanoelectrical transduction: review and perspectives *Polym. Int.* **59** 279–89

[17] Bhandari B, Lee G Y and Ahn S H 2012 A review on IPMC material as actuators and sensors: fabrications, characteristics and applications *Int. J. Precis. Eng. Manuf.* **13** 141–63

[18] Punning A, Kruusmaa M and Aabloo A 2007 A self-sensing ion conducting polymer metal composite (IPMC) actuator *Sensor Actuators* A **136** 656–64

[19] Kruusamäe K, Brunetto P, Punning A, Kodu M, Jaaniso R, Graziani S, Fortuna L and Aabloo A 2011 Electromechanical model for a self-sensing ionic polymer metal composite actuating device with patterned surface electrodes *Smart Mater. Struct.* **20** 124001

[20] Anton M, Kruusmaa M, Aabloo A and Punning A 2006 Validating usability of ionomeric polymer-metal composite actuators for real world applications *2006 IEEE/RSJ Int. Conf. on Intelligent Robots and Systems* (Piscataway, NJ: IEEE) pp 5441–5446

[21] Hunt A, Chen Z, Tan X and Kruusmaa M 2010 Control of an inverted pendulum using an ionic polymer-metal composite actuator *2010 IEEE/ASME Int. Conf. on Advanced Intelligent Mechatronics* (Piscataway, NJ: IEEE) pp 163–168

[22] Bhat N D 2004 Modeling and precision control of ionic polymer metal composite *Master's Thesis* Texas A&M University

[23] Chen Z and Tan X 2008 A control-oriented and physics-based model for ionic polymer-metal composite actuators *IEEE/ASME Trans. Mechatronics* **13** 519–29

[24] Mallavarapu K, Newbury K M and Leo D J 2001 Feedback control of the bending response of ionic polymer-metal composite actuators *SPIE's 8th Annual Int. Symp. on Smart Structures and Materials* vol 4329 pp 301–310

[25] Xing H L, Jeon J H, Park K C and Oh I K 2013 Active disturbance rejection control for precise position tracking of ionic polymer-metal composite actuators *IEEE/ASME Trans. Mechatronics* **18** 86–95

[26] Thinh N T, Yang Y-S and Oh I-K 2009 Adaptive neuro-fuzzy control of ionic polymer metal composite actuators *Smart Mater. Struct.* **18** 065016

[27] Chen Z, Kwon K-Y and Tan X 2008 Integrated IPMC/PVDF sensory actuator and its validation in feedback control *Sensors Actuators* A **144** 231–41

[28] Leang K K, Shan Y, Song S and Kim K J 2012 Integrated sensing for IPMC actuators using strain gages for underwater applications *IEEE/ASME Trans. Mechatronics* **17** 345–55

[29] Richardson R C, Levesley M C, Brown M D, Hawkes J A, Watterson K and Walker P G 2003 Control of ionic polymer metal composites *IEEE/ASME Trans. Mechatronics* **8** 245–53

[30] Kaneda Y, Kamamichi N, Yamakita M, Asaka K and Luo Z 2003 Control of linear artificial muscle actuator using IPMC *SICE 2003 Annual Conf.* vol 2 pp 1650–1655

[31] Kang S, Shin J, Kim S J, Kim H J and Kim Y H 2007 Robust control of ionic polymer-metal composites *Smart Mater. Struct.* **16** 2457–63

[32] Fang B-K, Ju M-S and Lin C-C K 2007 A new approach to develop ionic polymer-metal composites (IPMC) actuator: fabrication and control for active catheter systems *Sensors Actuators* A **137** 321–9

[33] Hao L, Sun Z, Li Z, Su Y and Gao J 2012 A novel adaptive force control method for IPMC manipulation *Smart Mater. Struct.* **21** 075016

[34] Lee G-Y, Choi J-O, Kim M and Ahn S-H 2011 Fabrication and reliable implementation of an ionic polymer-metal composite (IPMC) biaxial bending actuator *Smart Mater. Struct.* **20** 105026

[35] Newbury K M 2002 Characterization, modeling and control of ionic polymer transducers *PhD Thesis* Virginia Polytechnic Institute and State University

[36] Bonomo C, Fortuna L, Giannone P and Graziani S 2004 A sensor–actuator integrated system based on IPMCs *Sensors 2004. Proc. IEEE* (Piscataway, NJ: IEEE) pp 489–492

[37] Yamakita M, Sera A, Kamamichi N, Asaka K and Luo Z-W 2006 Integrated design of IPMC actuator/sensor *Proc. 2006 IEEE Int. Conf. on Robotics and Automation* (Piscataway, NJ: IEEE) pp 1834–1839

[38] Gonzalez C and Lumia R 2015 An IPMC microgripper with integrated actuator and sensing for constant finger-tip displacement *Smart Mater. Struct.* **24** 055011
[39] Hunt A, Chen Z, Tan X and Kruusmaa M 2009 Feedback control of a coupled IPMC (ionic polymer-metal composite) sensor–actuator *ASME 2009 Dynamic Systems and Control Conf.* pp 485–491
[40] Anton M, Aabloo A, Punning A and Kruusmaa M 2008 A mechanical model of a non-uniform ionomeric polymer metal composite actuator *Smart Mater. Struct.* **17** 025004
[41] Sadeghipour K, Salomon R and Neogi S 1992 Development of a novel electrochemically active membrane and 'smart' material based vibration sensor/damper *Smart Mater. Struct.* **1** 172–9
[42] Shahinpoor M and New A 1995 A new effect in ionic polymeric gels: the ionic flexofelectric effect *Smart Structures & Materials '95* (San Diego, CA) vol 2441 pp 42–53
[43] Konyo M, Konishi Y, Tadokoro S and Kishima T 2004 Development of velocity sensor using ionic polymer-metal composites *Proc. SPIE* **5385** pp 307–318 SPIE
[44] Farinholt K and Leo D J 2004 Modeling of electromechanical charge sensing in ionic polymer transducers *Mech. Mater.* **36** 421–33
[45] Chen Z, Tan X, Will A and Ziel C 2007 A dynamic model for ionic polymer-metal composite sensors *Smart Mater. Struct.* **16** 1477–88
[46] Bonomo C, Fortuna L, Giannone P, Graziani S and Strazzeri S 2006 A model for ionic polymer metal composites as sensors *Smart Mater. Struct.* **15** 749–58
[47] Shahinpoor M and Kim K J 2004 Ionic polymer-metal composites: III. Modeling and simulation as biomimetic sensors, actuators, transducers, and artificial muscles *Smart Mater. Struct.* **13** 1362–88
[48] Zhou K and Doyle J C 1998 *Essentials of Robust Control* (*Prentice Hall Modular Series for Eng*) (Englewood Cliffs, NJ: Prentice-Hall)
[49] Bibel J E and Malyevac D S 1992 *Guidelines for the Selection of Weighting Functions for H-Infinity Control* (Dahlgren, VA: Dahlgren Division of the Naval Surface Warfare Center)
[50] Timoshenko S 1940 *Strength of Materials: I. Elementary Theory and Problems* 2nd edn (New York: D. Van Nostrand Company, Inc.) pp 147–153 ch 35
[51] Li J, Wilmsmeyer K G, Hou J and Madsen L A 2009 The role of water in transport of ionic liquids in polymeric artificial muscle actuators *Soft Matter* **5** 2596–602
[52] Porfiri M 2009 An electromechanical model for sensing and actuation of ionic polymer metal composites *Smart Mater. Struct.* **18** 015016
[53] Punning A *et al* 2014 Lifetime measurements of ionic electroactive polymer actuators *J. Intell. Mater. Syst. Struct.* **25** 2267–75
[54] Nemat-Nasser S and Zamani S 2006 Modeling of electrochemomechanical response of ionic polymer-metal composites with various solvents *J. Appl. Phys.* **100** 064310